



Vibrational identification of Janus PtXO ($X = \text{S, Se}$) monolayers with strong out-of-plane piezoelectricity

Wei Zhang ^{1,*} and Weixiao Ji²

¹*Physicochemical Group of the School of Criminal Science and Technology & Forensic Center, Nanjing Police University, Nanjing 210023, China*

²*Spintronics Institute, School of Physics and Technology, University of Jinan, Jinan 250022, China*

 (Received 2 April 2023; revised 22 May 2023; accepted 6 July 2023; published 17 July 2023)

The breaking of structural symmetries make two-dimensional Janus materials have additional degrees of freedom that can lead to novel electronic and piezoelectric properties. Although Janus PtSSe and other analogous materials have recently been synthesized or predicted, the discovery of Janus piezoelectrics with large vertical piezoelectricity and a systematic understanding of the piezoelectricity of Pt-based Janus materials are still lacking. Here, we identify two new Janus piezoelectric PtXO ($X = \text{S, Se}$) monolayers with strong out-of-plane piezoelectricity by first-principles calculations. Unlike the symmetric binary systems, PtXO exhibit additional Raman-active modes and their activities can be regularly tuned by the biaxial compressive (tensile) strain, which simultaneously ensures the mechanic, dynamic, and thermal stabilities of PtXO. Notably, the out-of-plane $e_{31\text{S}}$ of PtXO are one order larger than those of Janus PtSSe, PtSTe, and PtSeTe. The electronic parts are found to play the dominant role in determining the piezoelectricity of all Pt-based Janus materials, based on which we reveal that the piezoelectric performances of Pt-based Janus materials are generally in proportion to the Bader charge difference and the electronegativity difference ratio of the two asymmetric layers. Moreover, the vertical piezoelectricity can be further enhanced by the compressive strain. Our results indicate that Janus PtXO are candidates for the potential applications on nanoscale piezoelectrics; the discussions about piezoelectricity would help to predict or design other transition metal dichalcogenide based Janus materials with strong out-of-plane piezoelectricity in advance.

DOI: [10.1103/PhysRevB.108.035411](https://doi.org/10.1103/PhysRevB.108.035411)

I. INTRODUCTION

Since the successful exfoliation of the well-known graphene [1,2], two-dimensional (2D) materials, e.g., the single-layer hexagonal boron nitride (BN) [3] and the monolayer transition metal dichalcogenides (TMDCs) [4], have attracted great attention [5–9] because of their novel physical properties and the potential for the device applications at the nanoscale. The structural formula of monolayer TMDCs is MX_2 , where M and X are respectively the transition metals (W, Mo, Pt, etc.) and the chalcogen elements (S, Se, Te, etc.). Among the family of TMDCs, monolayer MoS_2 is one of the most studied members. MoS_2 , which belongs to the D_{3h} point group, has the in-plane piezoelectricity but does not exhibit the out-of-plane piezoelectricity. Along the out-of-plane direction, the symmetric structure of pristine MoS_2 is also not beneficial to the spatial separation of photogenerated charge carriers.

Recently, researchers synthesized the Janus MoSSe monolayer [10,11], which sandwiched the middle Mo layer between two different chalcogen layers. More new 2D Janus materials have been discovered in subsequent theoretical and experimental work, e.g., In_2XY ($X, Y = \text{S, Se, Te}; X \neq Y$)

[12], WSSe [13], MoSTe [14], bilayer MoSSe [15], and PtSSe [16,17]. Very recently, the theoretically predicted [16] Janus PtSSe monolayer was experimentally synthesized by Sant *et al.* [17]. The lack of inversion symmetry and out-of-plane mirror symmetry make the 2D Janus materials have additional degrees of freedom to improve or tune the physical properties, including the out-of-plane piezoelectricity that is absent in pristine MX_2 monolayers. The piezoelectric materials with vertical piezoelectricity have broad application prospects, such as the human pulse diagnosis that can detect the weak vibration patterns of the human radial artery [18], the remote monitoring of intelligent robot motion, and the quantitative detection of pressure distributions [19]. Thus, it is important to explore suitable candidates for the piezoelectrics with strong vertical piezoelectricity.

Despite that these pioneer works used the X ($X = \text{S, Se, Te}$) atoms as the third component to design the TMDC-based Janus structures, the inclusion of oxygen in pristine TMDCs was less considered [20]. Experimentally, except for the well-known graphene oxide [21], the obtained PtS_2 treated by oxygen plasma was found to have the surface oxide layer by forming the Pt-O bonds [22]. In the Pt(111) single-crystal surface, two stable surface oxides were observed by the ReactorSTM [23]. In our previous work, Janus PtXO ($X = \text{S, Se}$) were found to be visible light driven water splitting photocatalysts with high carrier mobilities [24]. Compared with symmetric PtX_2 systems, the formation of

*Corresponding author: zhangw@nfpc.edu.cn; 284522094@qq.com

Janus PtXO enhanced the overpotentials of carriers, the photo-generated electrons/holes in Janus PtXO could be efficiently separated, and Janus PtSO globally had higher electron mobility than Janus PtSSe [16], which was beneficial for the photocatalytic water splitting [24]. However, the piezoelectric performances of PtXO had not been revealed so far. Although Janus PtSSe and other analogous Janus materials had been synthesized [17] or predicted [25], a systematic understanding of the piezoelectricity of Pt-based Janus materials is still lacking. Previous experiment found the 1L-TMDCs could sustain the strain up to about 11% [26]. Strain is a readily feasible knob to tailor the properties of 2D materials [27,28]. Considering that the Raman intensities and peak positions closely depend on the presence of strain [29], and Raman spectroscopy is a widely adopted technique for the characterization of 2D materials, it is therefore necessary to investigate the strain effects on the Raman peaks of Janus PtXO so as to stimulate further experiments. In this context, the following questions arise naturally which guide our first-principles calculations: Which vibrational modes of PtXO are Raman active? How do the Raman activities change with strain? Can PtXO keep the dynamic stability under strain? Does PtXO have considerable vertical piezoelectricity that is comparable to or even larger than other Pt-based Janus monolayers?

II. COMPUTATIONAL DETAILS

We perform the DFT calculations using the projector augmented wave (PAW) method [30] that is implemented in VASP [31,32]. The GGA in the form of Perdew-Burke-Ernzerhof (PBE) [33] is adopted as the exchange-correlation potential. A plane-wave cutoff energy of 600 eV is used throughout. In the structural relaxations, a $15 \times 15 \times 1$ k mesh [34] is used, and the force convergence criterion is 10^{-3} eV/Å. The van der Waals (vdW) correction is included using the DFT + D3 method [35,36]. The length of the c axis is set to 30 Å to avoid interactions of adjacent slabs. To get the phonon dispersion, we use PHONOPY [37] to construct the $8 \times 8 \times 1$ supercell with the framework of density functional perturbation theory (DFPT). To obtain the relaxed-ion piezoelectric tensors, the DFPT is used based on the rectangle cell shown in Figs. 1(a) and 1(b). During the phonon and piezoelectricity calculations, the total energy is converged to 10^{-8} eV.

According to the Placzek approximation, the Raman activity (R_a) of a Raman-active phonon mode is proportional to $|\vec{e}_i \cdot \mathbf{R} \cdot \vec{e}_s|^2$, where the vectors \vec{e}_i and \vec{e}_s respectively represent the polarization direction of the incident light and the scattering light. \mathbf{R} is Raman tensor, which is a 3×3 second-rank tensor,

$$\begin{bmatrix} \frac{\partial P_{xx}}{\partial q_i} & \frac{\partial P_{xy}}{\partial q_i} & \frac{\partial P_{xz}}{\partial q_i} \\ \frac{\partial P_{yx}}{\partial q_i} & \frac{\partial P_{yy}}{\partial q_i} & \frac{\partial P_{yz}}{\partial q_i} \\ \frac{\partial P_{zx}}{\partial q_i} & \frac{\partial P_{zy}}{\partial q_i} & \frac{\partial P_{zz}}{\partial q_i} \end{bmatrix}. \quad (1)$$

The element of \mathbf{R} is the derivative of a material's polarizability with respect to the i th phonon mode q_i , which is calculated by the finite-difference method. The Raman activity R_a is

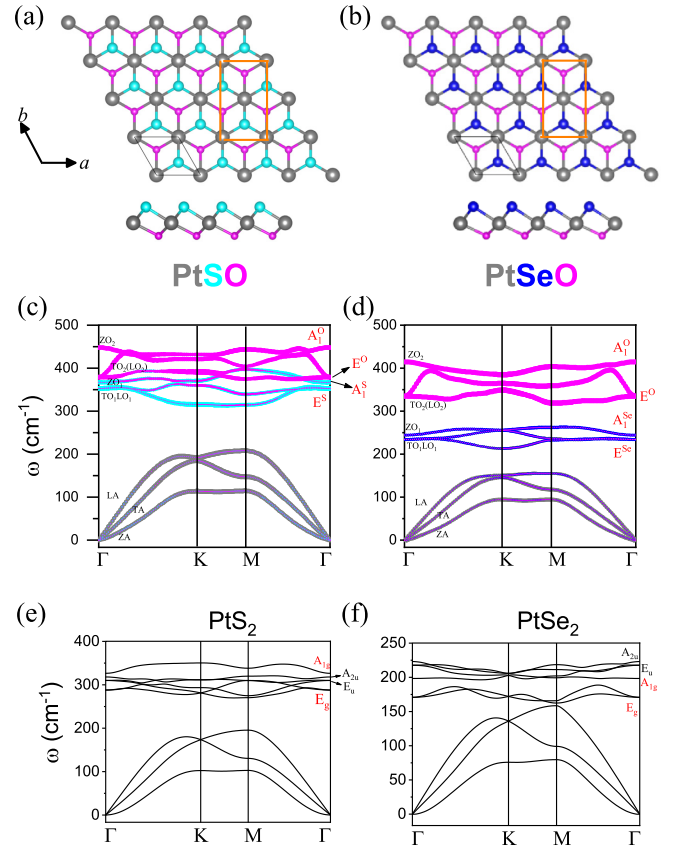


FIG. 1. (a) Top view and side view of the crystal structures of Janus PtXO ($X = S, Se$). The hexagonal primitive cells and the rectangle cells are respectively marked by black lines and orange lines. (b), (c) The phonon dispersion of PtXO and PtX₂. The gray, cyan, blue, and magenta not only denote the Pt, S, Se, and O atoms in (a), but also denote the contributions to phonon modes in (b). The Raman-active modes are marked by red fonts in (b) and (c). LO (TO) denotes the longitudinal (transverse) optical phonon.

represented by the Raman invariants,

$$R_a = 45\alpha^2 + 7\beta^2, \quad (2)$$

where α and β are respectively the isotropic and anisotropic parts of \mathbf{R} ,

$$\alpha = \frac{1}{3}(R_{xx} + R_{yy} + R_{zz}), \quad (3)$$

$$\beta^2 = \frac{1}{2}[(R_{xx} - R_{yy})^2 + (R_{xx} - R_{zz})^2 + (R_{yy} - R_{zz})^2 + 6(R_{xy}^2 + R_{xz}^2 + R_{yz}^2)]. \quad (4)$$

III. RESULTS

A. Phonon vibration modes and Raman activity

We first recall the basic structural properties of Janus PtXO ($X = S, Se$). The relaxed crystal structures shown Figs. 1(a) and 1(b) are obtained based on the pristine PtX₂ ($X = S, Se$) monolayers [38–40], where the X atom of one side is replaced by the O atom. The calculated lattice constants of Janus PtSO and PtSeO are respectively 3.37 and 3.47 Å. The bond lengths Pt- X ($X = S, Se$) are slightly larger than that of Pt-O, suggesting more distinctive properties than the symmetric

PtX₂ monolayers. More details of the structural parameters and related mechanical and electronic properties are given in Table S1 of Supplemental Material [41] (SM hereafter).

Figures 1(c) and 1(d) show the site-projected phonon dispersions of PtXO. Being free of imaginary frequencies in the whole Brillouin zone demonstrates the dynamic stability of the two structures. With the increase of mass of the chalcogen atom, the vibration frequencies of nine phonon modes decrease from PtSO to PtSeO. At the Γ point, the lowest three branches are the acoustic modes (ZA, LA, TA); the rest six branches are all optical modes, among which LO₁/TO₁ and LO₂/TO₂ are doubly degenerate. The acoustic modes mainly originate from the vibrations of the heavy Pt atom. Differently from the case of PtX₂ [Figs. 1(e) and 1(f)], where the optical modes are mainly contributed by the X atom with a small mixture of Pt atom (not shown), the highest optical modes (ZO₂, LO₂/TO₂) in PtXO are mainly contributed by the O atom, and the optical modes (ZO₁, LO₁/TO₁) with lower frequency mainly consist of the X atom. The crystal structures of pristine PtX₂ monolayers belong to the D_{3d} point group (Schoenflies notation). The irreducible representations [42] of the optical modes are E_g , E_u , A_{1g} , and A_{2u} , where E_g and E_u denote the in-plane vibrations of the doubly degenerate phonon modes while A_{1g} and A_{2u} denote the modes with out-of-plane vibrations. Among these modes, only E_g and A_{1g} are Raman-active which are marked by red in Figs. 1(e) and 1(f). However, there are two additional Raman-active modes in Janus PtXO with the C_{3v} point group symmetry; the corresponding irreducible representations of Raman-active modes are $2A + 2E_1$ [42], which are marked by A_1^S (A_1^{Se}), A_1^O , E^S (E^{Se}), and E^O for clarity. Figure 2 shows the Raman spectrum and atoms vibrations of Raman-active modes for PtS₂ and PtXO ($X = S, Se$). We can see that the E_g and A_{1g} Raman modes in PtS₂ respectively correspond to the out-of-plane and in-plane opposite vibrations of two S atoms with the same amplitude, while the Pt atom is still in two Raman modes. PtSe₂ exhibits similar vibrations for E_g and A_{1g} except for the difference of peak positions. The E_g (A_{1g}) of PtS₂ and PtSe₂ respectively locate at 288.27 (326.2) and 170.77 (198.27) cm^{-1} . For both of PtS₂ and PtSe₂, the Raman activity of E_g is much larger than that of A_{1g} . These results are generally consistent with previous experiments [43,44]; see Table S2 of the SM for the detailed comparisons with experiments and the expected experimental Raman frequencies of PtXO. In the Janus PtXO, the Pt atom that is static in PtX₂ now vibrates with small amplitude in all the Raman modes. Besides the Pt atom, the E^S (E^{Se})/ A_1^S (A_1^{Se}) correspond to the opposite in-plane/out-of-plane vibrations of S (Se) and O atoms with different amplitudes; they are mainly contributed by the S (Se) atom. The E^O / A_1^O denotes the in-plane/out-of-plane vibrations of S (Se) and O atoms in the same direction; they mainly arise from the vibration of the O atom. As shown in Fig. 2(c), the Raman activity of A_1^O of PtSO is on the order of 10^{-1} , which is two to three orders of magnitude smaller than other three Raman modes; the small Raman activity of A_1^O is attributed to the small change of in-plane polarizability (see Table S3 for details). In the PtSeO, the Raman activities of all active modes are on the order of 10^2 . The Raman activity of A_1^O in PtSeO is larger than E^O ; this is because the change of in-plane polarizability induced by A_1^O is larger than that of E^O (Table S3). The above results

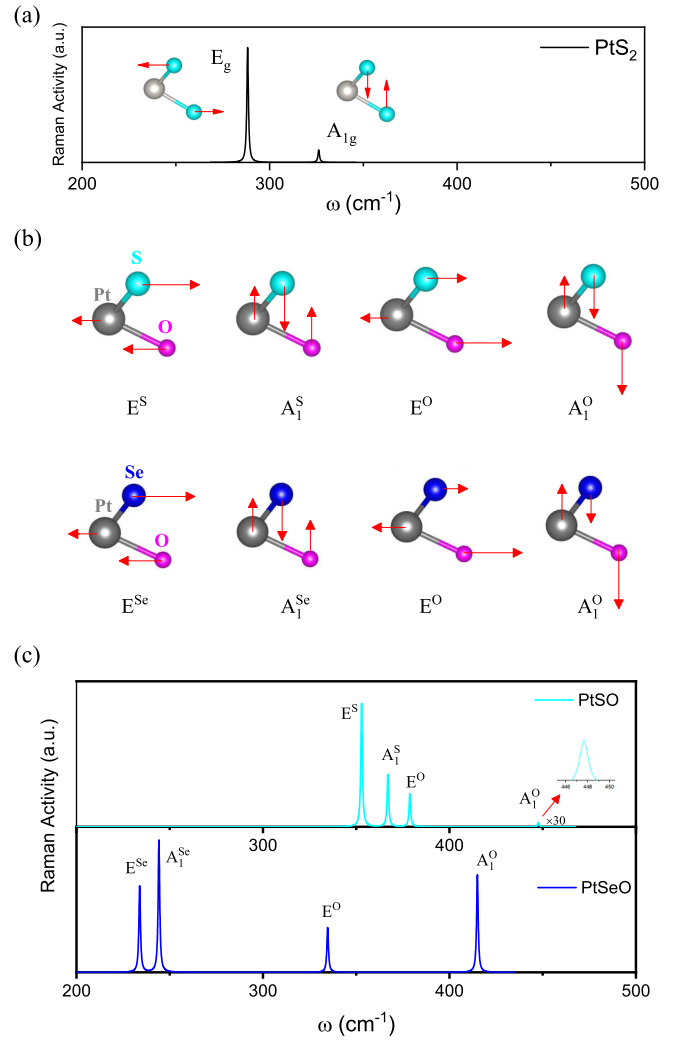


FIG. 2. Raman spectrum and atoms vibrations of Raman-active modes for (a) PtS₂ and (b), (c) PtXO ($X = S, Se$). The arrow length schematically illustrates the relative vibration amplitude of each atom.

indicate that the A_1^O of PSO may not be a prominent Raman peak in the unstrained condition, while other Raman modes can be observed by the experiments.

B. Dynamic stability and Raman shifts

The Raman peak positions and activities are closely related to the strain; we thus calculate the phonon dispersions of PtXO under biaxial strain ϵ , which is defined as the percentage value of $(a - a_0)/a_0$. a and a_0 are the unstrained and strained lattice constants, respectively. As shown in Fig. 3, all the frequencies are positive in the whole Brillouin zone, demonstrating that Janus PtXO are dynamically stable in the biaxial strain range of $-4\% \sim 10\%$. Considering that ϵ of 10% is a relative large strain in practice, we focus on reporting results in a moderate strain range of $-4\% \sim 6\%$ below unless otherwise stated. To further check the structural stabilities of PtXO under the strain, the *ab initio* molecular dynamics calculations are performed at 300 K using the canonical ensembles. The time step and the simulation time are respectively 1 fs and 10 ps. As shown in

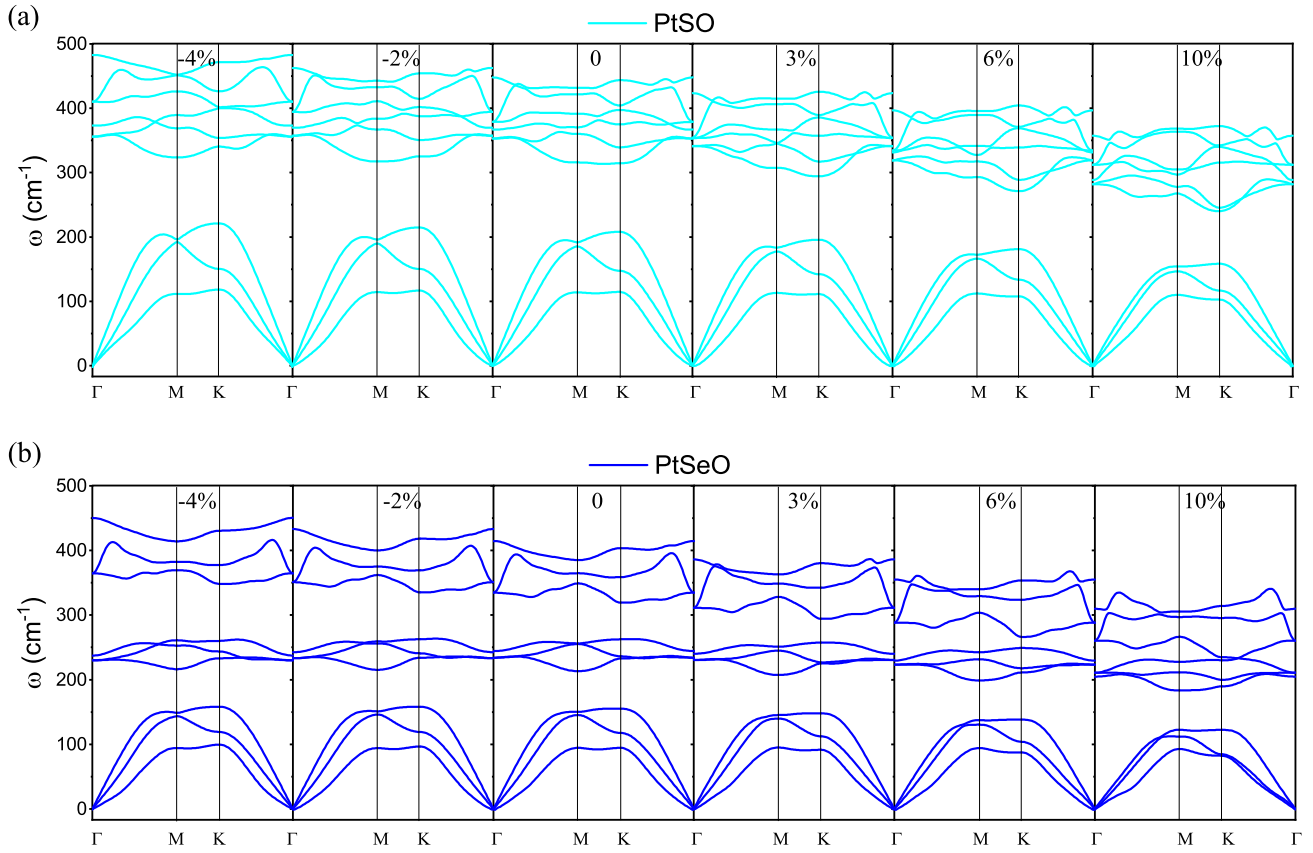


FIG. 3. Phonon dispersions of Janus PtXO ($X = S, \text{Se}$) under the in-plane biaxial strain.

Fig. S1 of the SM, the free energies of PtSO and PtSeO under ϵ of -4% and 6% fluctuate slightly around the fixed values; the obtained structures at 10 ps maintain their morphologies, indicating the strained Janus PtXO are thermally stable at room temperature.

Figures 4(a) and 4(b) show the phonon frequency shifts of Raman-active modes of Janus PtXO under biaxial strain. It can be seen that the tensile (compressive) strain softens (hardens) the frequencies of A_1^O and E^O . The A_1^S (A_1^{Se}) and E^S (E^{Se}) display phonon softening when the compressive strain is larger than $\sim -2\%$. To understand the different responses of Raman modes to the strain, we first calculate the Grüneisen parameter $\gamma(q)$ in the $q = 0$ limit,

$$\gamma(q) = -\frac{a_0}{2\omega_0^q} \left[\frac{\omega_+^q - \omega_-^q}{a_+ - a_-} \right], \quad (5)$$

where a_0 (ω_0^q) is the unstrained lattice constant (phonon frequency), and a_+ (a_-) and ω_+^q (ω_-^q) respectively denote the lattice constant and phonon frequency under the tensile (compressive) strain. The calculated $\gamma(E^O)$, $\gamma(A_1^O)$, $\gamma(E^S)$, and $\gamma(A_1^S)$ are respectively 1.08, 0.87, 0.43, and 0.39 in PtSO, and $\gamma(E^O)$, $\gamma(A_1^O)$, $\gamma(E^{\text{Se}})$, and $\gamma(A_1^{\text{Se}})$ are respectively 1.2, 1.12, 0.12, and 0.07 in PtSeO, i.e., $\gamma(E^O) > \gamma(A_1^O) > \gamma(E^S) > \gamma(A_1^S)$ and $\gamma(E^O) > \gamma(A_1^O) > \gamma(E^{\text{Se}}) > \gamma(A_1^{\text{Se}})$, which reflect the small frequency shift of E^S (E^{Se}) and A_1^S (A_1^{Se}) around the Γ point. Specially, the γ s of modes dominated by oxygen, i.e., $\gamma(E^O)$ and $\gamma(A_1^O)$, are pronouncedly larger

than the γ s of modes dominated by chalcogens, i.e., $\gamma(E^S)$, $\gamma(E^{\text{Se}})$, $\gamma(A_1^S)$, and $\gamma(A_1^{\text{Se}})$. $\gamma(E^O)$ and $\gamma(A_1^O)$ are larger than the $\gamma(0.21 \sim 0.68)$ [45,46] of Raman-active modes of MX_2 ($M = \text{Mo/W}$, $X = \text{S/Se}$); $\gamma(E^S)$, $\gamma(E^{\text{Se}})$, $\gamma(A_1^S)$, and $\gamma(A_1^{\text{Se}})$ are comparable with that of MX_2 . Next, we plot the evolution of bond length (d) with respect to strain in Fig. S2. We can see the compressive strain continuously decreases the $d_{\text{Pt-O}}$ at a constant slope, whereas the decrease rate of $d_{\text{Pt-S}}$ ($d_{\text{Pt-Se}}$) is much smaller than that of $d_{\text{Pt-O}}$. The A_1^S (A_1^{Se}) and E^S (E^{Se}) mainly come from the contribution of the S (Se) atom; thus the nearly unchanged $d_{\text{Pt-S}}$ ($d_{\text{Pt-Se}}$) at large compressive strain restricts the increase of vibration strength of S (Se) atom. Contrarily, the tensile strain simultaneously enlarges $d_{\text{Pt-S}}$ ($d_{\text{Pt-Se}}$) and $d_{\text{Pt-O}}$, resulting in the continuous softening of phonon frequency.

Figures 4(c) and 4(d) show the evolution of Raman activity. In the strain range of $\epsilon < 6\%$, the compressive strains in both PtSO and PtSeO prefer to remarkably enhance the activities of E^S (E^{Se}) and A_1^S (A_1^{Se}), while the tensile strains prefer to remarkably enhance the activities of E^O (A_1^O) in PtSO and A_1^O of PtSeO. In PtSO, the A_1^O which is not prominent at $\epsilon = 0$ becomes one of the main peaks at $\epsilon = 4\%$. In PtSeO, the tensile strain has little influence on the activity of E^O comparing with other Raman modes. The compressive strain tends to increase the height between the S (Se) layer and the oxygen layer; the tensile strain tends to stretch the two asymmetric layers; and the above results suggest that the tensile strain and compressive strain induced structural changes respectively

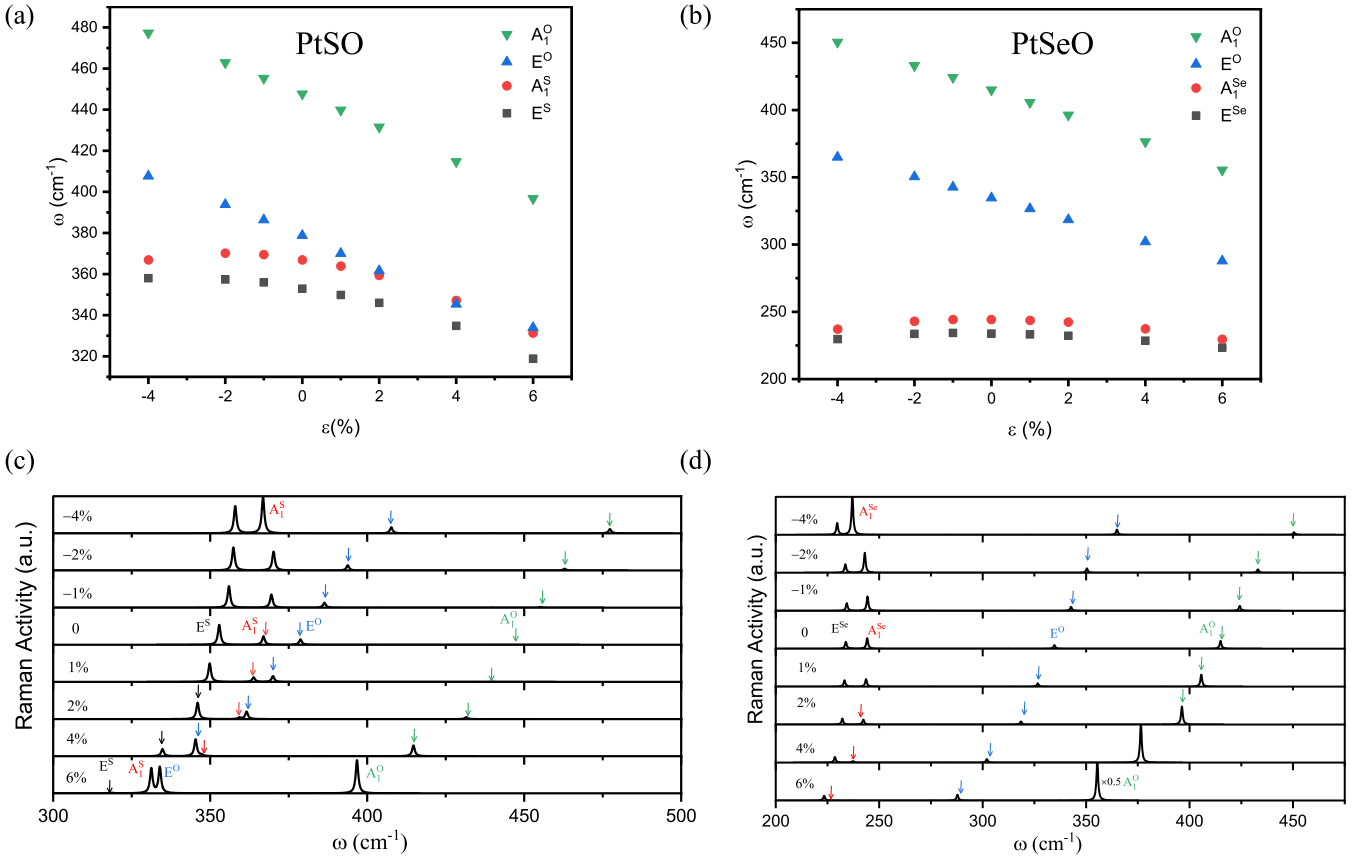


FIG. 4. (a), (b) The phonon frequency shifts of Raman-active modes of Janus PtXO ($X = S, Se$) under the biaxial strain. (c), (d) The evolution of Raman activities. The arrows with different colors denote the peak positions of different modes. The same scales of R_a are used for the subgraphs of (c) or (d).

increase the polarizability of A_1^O and E^X (A_1^X) ($X = S, Se$). When $\epsilon \geq 6\%$, e.g., the case of PtSO at $\epsilon = 6\%$, the activity of A_1^S suddenly increases. Further tests (Fig. S3) show that both A_1^S and A_1^{Se} significantly increase at $\epsilon = 10\%$, reflecting the large tensile strain induced different effects on Raman activity compared with the case of smaller strain. The regular response of Raman activity in the strain range of $-4\% \sim 4\%$, together with the phonon frequency shift, indicate that the strain can be monitored by tracking the change of modes activities and peak positions.

C. Piezoelectricity of monolayer PtXO

The lack of an inversion center between Pt and X ($X = S, Se$) layers suggests that Janus PtXO have certain quantitative out-of-plane piezoelectricity. Moreover, a piezoelectric material should be an insulator. The electronic band gap obtained by HSE06 is 2.5 (1.85) eV for PtSO (PtSeO), indicating the insulator characteristic of PtXO. The third-rank piezoelectric stress tensor e_{ijk} and piezoelectric strain tensor d_{ijk} are respectively calculated by

$$e_{ijk} = \frac{\partial P_i}{\partial \epsilon_{jk}} = e_{ijk}^{\text{ion}} + e_{ijk}^{\text{elec}}, \quad (6)$$

$$d_{ijk} = \frac{\partial P_i}{\partial \sigma_{jk}} = d_{ijk}^{\text{ion}} + d_{ijk}^{\text{elec}}, \quad (7)$$

where *ion* and *elec* respectively denote the ionic and electronic contributions to corresponding piezoelectric tensors, and ϵ_{jk} , σ_{jk} , and P_i are respectively the strain tensor, the stress tensor, and the polarization vector. Using Voigt's notation, the e_{ijk} becomes [47]

$$\begin{bmatrix} e_{11} & -e_{11} & 0 \\ 0 & 0 & -e_{11} \\ e_{31} & e_{31} & 0 \end{bmatrix}; \quad (8)$$

e_{31} and e_{11} respectively denote the polarization in the z and x directions induced by the strain along the x direction. e_{11} and e_{31} are directly obtained by DFPT; d_{11} and d_{31} are calculated by the relation $e = dC$, where C is the elastic tensor,

$$d_{11} = \frac{e_{11}}{C_{11} - C_{12}}, \quad (9)$$

$$d_{31} = \frac{e_{31}}{C_{11} + C_{12}}. \quad (10)$$

Table I shows the calculated elastic constants of PtXO. For comparison we also report the results of other Pt-based 2D Janus materials, including the experimentally synthesized Janus PtSSe [17]. As a benchmark, we reproduce the piezoelectric coefficients of MoSSe in Table II. The calculated results in Tables I and II agree with previous work [16,25,39], ensuring the reliability of subsequent calculations of d_{11} and d_{31} . The calculated e_{11} (d_{11}) and e_{31} (d_{31}) are given in Table II

TABLE I. The calculated lattice constants a (Å), elastic constants C_{ij} (N m⁻¹), Young's modulus Y (N m⁻¹), and Poisson's ratio (ν) of PtXO ($X = S, Se$) and other Pt-based Janus materials.

	a	C_{11}	C_{12}	C_{66}	Y	ν
PtSO	3.37	95.22	25.33	34.94	88.48	0.27
PtSeO	3.47	71.15	19.78	25.69	65.65	0.28
PtSSe	3.64	78.07	21.17	28.45	72.33	0.27
	3.66 ^a	77.78 ^a	22.37 ^a	27.24 ^a	71.25 ^a	0.29 ^a
	3.66 ^b	77.56 ^b	20.31 ^b	28.62 ^b	72.24 ^b	0.26 ^b
PtSTe	3.77	67.83	18.07	24.88	63.02	0.27
	3.81 ^c	65.62 ^c	17.36 ^c	24.13 ^c	61.02 ^c	0.27 ^c
PtSeTe	3.85	66.73	18.82	23.95	61.42	0.28
	3.89 ^c	65.89 ^c	17.8 ^c	24.04 ^c	61.08 ^c	0.27 ^c

^aRef. [39];

^bRef. [16];

^cRef. [25].

and Figs. 5(a) and 5(b). PtSeO has larger e_{11} (d_{11}) and e_{31} (d_{31}) than PtSO. The e_{11} and d_{11} of PtSeO reach 4.52×10^{-10} C/m and 8.8 pm/V. The d_{11} of PtSeO are far larger than some typical 2D materials, e.g., Janus MoSSe [48], Janus MoSTe [14], WS₂ [49], and MoS₂ [49]. In Pt-based Janus systems, the (C_{11} - C_{12})s are on the same order of magnitude. However, the e_{11} s of PtXO are one order of magnitude larger than most of other Pt-based materials; PtSeO with smaller (C_{11} - C_{12}) has larger e_{11} than PtSO, resulting in the largest d_{11} . In other systems with smaller d_{11} than PtSeO, though BiTeI has smaller (C_{11} - C_{12}) [47]; their e_{11} s are all smaller than PtSeO, indicating the large e_{11} of PtSeO plays the dominant role in determining the larger d_{11} than other 2D systems. Significantly, PtXO show large out-of-plane piezoelectricity. Especially for the PtSeO, the e_{31} and d_{31} reach 1.4×10^{-10} C/m and 1.54 pm/V, which not only have the same order of magnitude as e_{11} and d_{11} , but also are one order larger than that of Janus MoSSe [48] and Janus MoSTe [14]. Moreover, Figs. 5(a) and 5(b) clearly show that PtXO have the largest piezoelectric coefficients among the Pt-based 2D Janus materials; e.g., the e_{31} s of PtXO are one

TABLE II. The comparisons of piezoelectric coefficients between PtXO and other 2D systems. The units of e_{ij} and d_{ij} are respectively 10^{-10} C/m and pm/V.

	e_{11}	d_{11}	e_{31}	d_{31}
PtSO	3.01	4.3	1.11	0.92
PtSeO	4.52	8.8	1.4	1.54
MoSSe	3.8	3.91	0.33	0.21
	3.89 ^a	4.24 ^a	0.42 ^a	0.29 ^a
SbTeI	2.71	13.03	0.13	0.36
	2.69 ^b	12.95 ^b	0.13 ^b	0.36 ^b
BiTeI	1.56 ^b	8.2 ^b	0.23 ^b	0.66 ^b
MoSTe	4.5 ^c	5.1 ^c	0.5 ^c	0.4 ^c
WS ₂	2.4 ^d	2.12 ^d		
MoS ₂	3.62 ^d	3.65 ^d		

^aRef. [48];

^bRef. [47];

^cRef. [14];

^dRef. [49].

order larger than those of Janus PtSSe, PtSTe, and PtSeTe. The strong out-of-plane piezoelectric coefficients indicate that Janus PtXO are candidates for the potential applications on touch-sensor nanodevices and ultrathin piezoelectric devices. To understand the large out-of-plane e_{31} of PtXO, we first analyze the ionic and electronic contributions to e_{31} in Fig. 5(c). We can see that the electronic parts play the dominant role in determining the e_{31} s of all the Pt-based Janus materials, which is different from some Janus materials such as SbTeI and BiTeI [47], where the e_{31} s mainly come from the ionic contributions. The dominant role of electronic contributions stimulate us to perform the Bader charge analysis [50] and plot the differential charge density in Fig. 6, which supports us in finding that the piezoelectricity of Pt-based Janus materials is closely related to the asymmetric charge transfer and the electronegativity difference ratio [Fig. 5(d)], which will be discussed later.

The main findings of Fig. 6 can be summarized by the following points: (i) The differential charge density is qualitatively consistent with the results of Bader charges. There is obviously more charge transfer between the cations and anions in PtXO; therefore the Bader charges (Q) of each atom in PtXO are larger than that of the rest three Janus materials. (ii) The asymmetric transfer of charges. The Bader charges of chalcogens reflect the charge transfer between the chalcogens and Pt. All the Pt-based Janus materials exhibit the character of asymmetric charge transfer between the up and down layers; e.g., the Bader charges of S and O in PtSO are respectively 0.11 and 0.76 e^- . (iii) The relative magnitudes of electronegativity (χ) between atoms determine the accumulation or depletion of electrons. For example, the Bader charges of Pt are all negative (i.e., loss of electrons) in PtXO and PtSSe, while they are all positive (i.e., gain of electrons) in PtSTe and PtSeTe. The χ s of Pt, O, S, Se, and Te are respectively 2.28, 3.44, 2.58, 2.55, and 2.1. In PtXO and PtSSe, χ (Pt) is smaller than χ (O), χ (S), and χ (Se). However, χ (Pt) is larger than χ (Te) in PtSTe and PtSeTe. Therefore the Pt atom prefers to obtain or lose electrons in different Pt-based Janus materials. χ (O) is the largest among these elements; thus the positive Bader charges of O are much larger than other chalcogens. The asymmetric charge transfer of the up and down layers can affect the electronic polarization; we thus propose two indices [inset of Fig. 5(d)], the Bader charge difference (ΔQ_{X-Y}) and the electronegativity difference ratio ($\Delta \chi_{\max}/\Delta \chi_{\min}$) between the up and down layers,

$$\Delta Q_{X-Y} = |Q_X - Q_Y|, \quad (11)$$

$$\frac{\Delta \chi_{\max}}{\Delta \chi_{\min}} = \frac{(|\chi(X) - \chi(M)|, |\chi(Y) - \chi(M)|)_{\max}}{(|\chi(X) - \chi(M)|, |\chi(Y) - \chi(M)|)_{\min}}; \quad (12)$$

$|Q_X - Q_Y|$ is the absolute value of $Q_X - Q_Y$. $\Delta \chi_{\max}$ and $\Delta \chi_{\min}$ are respectively the maximum and minimum values between $|\chi(X) - \chi(M)|$ and $|\chi(Y) - \chi(M)|$, and M represents the middle transition metal (i.e., Pt here). As shown in Fig. 5(d), the e_{31} s of all the Pt-based Janus materials are generally in proportion to the ΔQ_{X-Y} and $\Delta \chi_{\max}/\Delta \chi_{\min}$. The larger the ΔQ_{X-Y} and $\Delta \chi_{\max}/\Delta \chi_{\min}$ are, the stronger the e_{31} is. Notably, the ΔQ_{X-Y} and $\Delta \chi_{\max}/\Delta \chi_{\min}$ of PtSeTe are a little larger than that of PtSSe, but the e_{31} of PtSeTe is a little smaller than PtSSe. This can be attributed to the

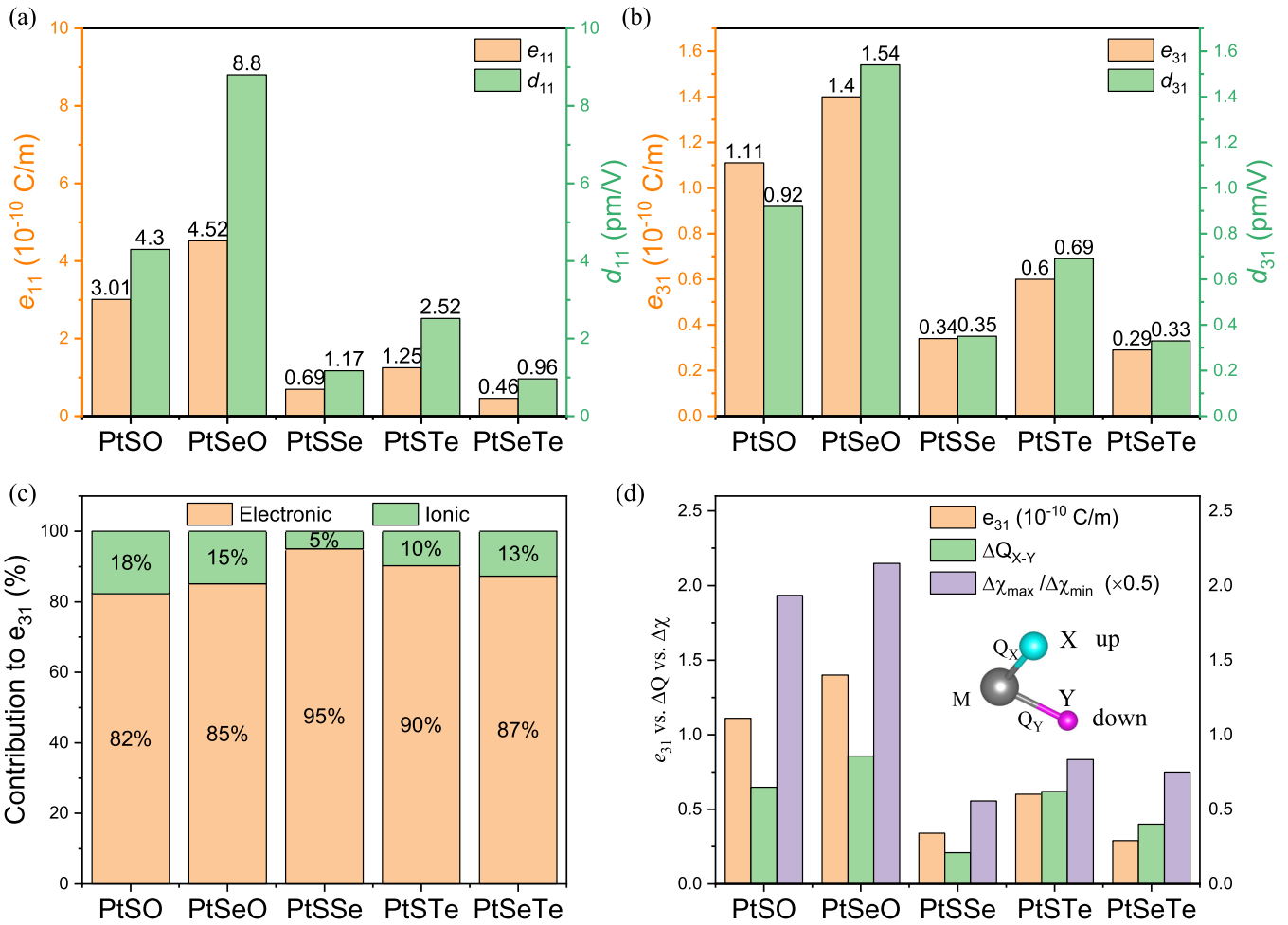


FIG. 5. The piezoelectric stress (strain) coefficients e_{ij} (d_{ij}) of Janus PtXO ($X = S, Se$) and other Pt-based Janus materials. The units of e_{ij} and d_{ij} are respectively 10^{-10} C/m and pm/V. Inset schematically shows the side view of basic structure of TMDC-based Janus materials. M denotes the metal, X and Y are the chalcogens, and $X \neq Y$.

different electronic contributions. The two materials' electronic parts of e_{31} are close to each other (PtSeTe/PtSSe, $0.34/0.36 \times 10^{-10}$ C/m); the electronic contribution to total

e_{31} is larger in PtSSe (95%) than in PtSeTe (87%). We wish to point out that the relation found here is not a strict guarantee that determines the exact quantitative relation of e_{31} s for all

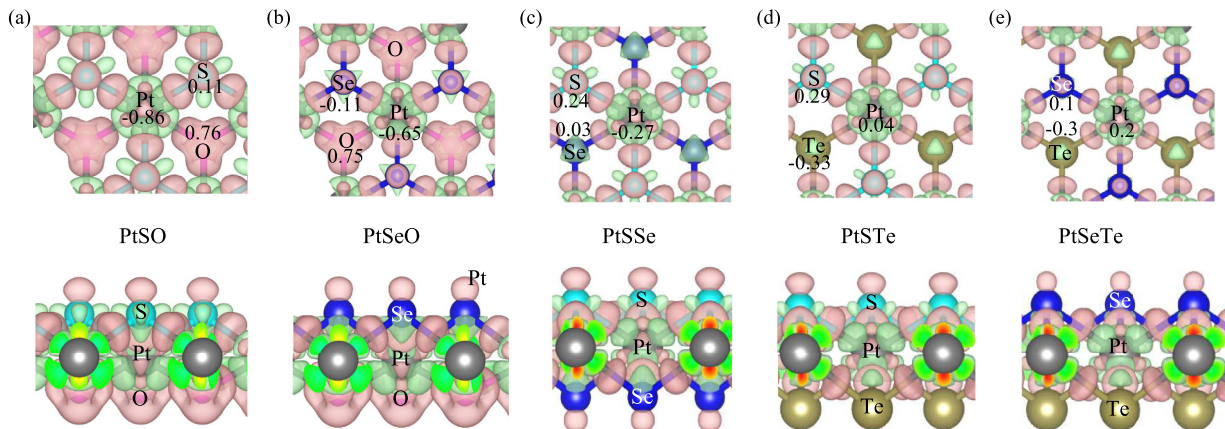


FIG. 6. The differential charge density and the Bader charges of Janus PtXO ($X = S, Se$), PtSSe, PtSTe, and PtSeTe. The positive (negative) values of Bader charges denote the gain (loss) of electrons. The light green (red) regions denote the depletion (accumulation) of electrons. The isosurface value is $0.01 e^-/\text{bohr}^3$ in all figures.

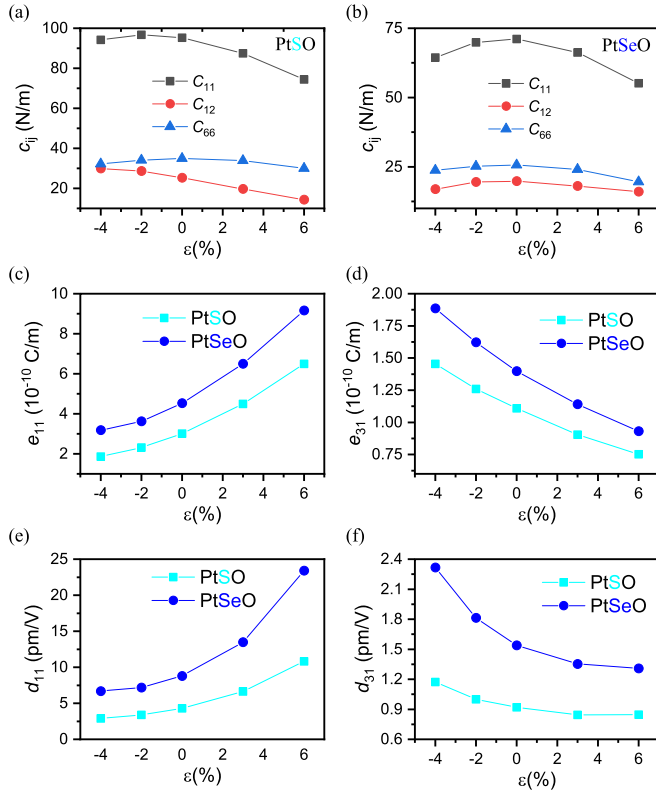


FIG. 7. The strain-dependent elastic constants (C_{ij}) and piezoelectric stress (strain) coefficients e_{ij} (d_{ij}) of Janus PtXO ($X = S, \text{Se}$). ϵ is the biaxial strain.

the Janus materials; the piezoelectric properties such as the strain coefficients are affected by the elastic constants, which are also related to the charge transfer and the electronegativity, and thus the two indices (ΔQ_{X-Y} , $\Delta \chi_{\max}/\Delta \chi_{\min}$) can provide guidance to predict or design TMDC-based Janus materials (MXY , $X \neq Y$) with strong out-of-plane piezoelectricity in advance.

D. Strain tunable piezoelectricity and piezoelectricity of bilayer PtSeO

Finally, the strain effects on the piezoelectricity are studied. As shown in Figs. 7(a) and 7(b), the elastic constants satisfy the Born criteria $C_{11}C_{22} - C_{12}^2 > 0$, $C_{66} > 0$, indicating PtXO are mechanically stable in the strained condition. Figures 7(c)–7(f) show that the piezoelectric coefficients of PtXO can be continuously tuned by the biaxial strain. The strain is more effective in tuning the piezoelectric coefficient of PtSeO than that of PtSO, as can be seen from the larger slope (absolute value) of PtSeO. The tensile strain can significantly enhance the e_{11} (d_{11}) while the compressive strain can effectively enhance the e_{31} (d_{31}). For example, the e_{11} of PtSeO at $\epsilon = 6\%$ is 9.16×10^{-10} C/m, which is twice as large as the case without strain; the corresponding d_{11} at $\epsilon = 6\%$ is 23.39 pm/V which is one order of magnitude larger than the case of $\epsilon = 0$; the e_{31} (d_{31}) of PtSeO increases from 1.4×10^{-10} C/m (1.54 pm/V) to 1.89×10^{-10} C/m (2.32 pm/V) at $\epsilon = -4\%$. Although the tensile strain and the compressive strain behave differently in tuning e_{11} (d_{11}) or e_{31}

(d_{31}), the overall decrease rates of e_{11} (d_{11}) (by compressive strain) and e_{31} (d_{31}) (by tensile strain) are respectively smaller than the increase rates of e_{31} (d_{31}) (by compressive strain) and e_{11} (d_{11}) (by tensile strain), especially for the case of d_{11} (d_{31}) of PtSeO, indicating that strain can effectively enhance the in-plane (out-of-plane) piezoelectric coefficients without losing too much the out-of-plane (in-plane) piezoelectric performance at the same time.

Stimulated by the fact that PtSeO has larger piezoelectric coefficients than PtSO, we construct the bilayer PtSeO to study the piezoelectric performances. As shown in Fig. S4 of the SM, six stacking patterns are considered. The binding energy (E_b) is calculated using

$$E_b = (E_{\text{bilayer}} - 2E_{1\text{L}})/S, \quad (13)$$

where E_{bilayer} and $E_{1\text{L}}$ are respectively the total energies of bilayer and monolayer PtSeO, and S is the surface area. The E_b s of all the six stacking patterns are negative, implying that the formation of bilayer is exothermic. The AA pattern is the ground state with an E_b of -43.96 meV/Å², the e_{11} is 6.46×10^{-10} C/m which is larger than that of monolayer, and the e_{31} reaches 2.67×10^{-10} which is twice as much as the case of monolayer. For other patterns, their e_{11} (e_{31}) maximally reaches 7.71×10^{-10} (2.87×10^{-10}) C/m. Therefore the formation of bilayer PtSeO would enhance the piezoelectric stress coefficients.

IV. CONCLUSION

In summary, using the first-principles calculations, two new Janus piezoelectric PtXO ($X = S, \text{Se}$) monolayers with strong out-of-plane piezoelectricity are discovered by studying the phonon dispersions, the *ab initio* molecular dynamics, the Raman activities, the piezoelectricity, the charge transfer and the related strain effects. Distinct from the symmetric PtX₂ systems, two additional Raman-active modes are identified in PtXO. The biaxial compressive (tensile) strain not only can regularly tune the Raman activities, but also simultaneously keep the mechanic, dynamic, and thermal stabilities of PtXO. Importantly, we find the out-of-plane piezoelectric coefficient e_{31} s of PtXO are one order larger than that of other Pt-based Janus materials, including Janus PtSSe, PtSTe, and PtSeTe. It is found the piezoelectricity of Pt-based Janus materials mainly comes from the contribution of the electronic parts. We reveal that the piezoelectric performances of Pt-based Janus materials are generally in proportion to the Bader charge difference and the electronegativity difference ratio of the two asymmetric layers. Besides, the vertical piezoelectricity can be further enhanced by the compressive strain. Our results not only show that Janus PtXO are candidates for the potential applications on nanoscale piezoelectrics, but also provide guidance for the prediction or design of other TMDCs-based Janus materials with strong out-of-plane piezoelectricity in advance.

ACKNOWLEDGMENTS

W.Z. and W.J. are supported by National Natural Science Foundation of China (Grants No. 11704189 and No. 11804116). W.Z. is also sponsored by the excellent scien-

tific and technological innovation team of higher education in Jiangsu Province (Grant No. 2019-29). W.J. is also sponsored by the Natural Science Foundation of Shandong Province

(Grant No. ZR2018QA006). Calculations are performed at the Shanghai Supercomputer Center (SSC) and Sunway TaihuLight National Supercomputer Center.

- [1] K. S. Novoselov, A. K. Geim, S. V. Morozov, D. Jiang, Y. Zhang, S. V. Dubonos, I. V. Grigorieva, and A. A. Firsov, *Science* **306**, 666 (2004).
- [2] K. S. Novoselov, A. K. Geim, S. V. Morozov, D. Jiang, M. I. Katsnelson, I. V. Grigorieva, S. V. Dubonos, and A. A. Firsov, *Nature (London)* **438**, 197 (2005).
- [3] C. R. Dean, A. F. Young, I. Meric, C. Lee, L. Wang, S. Sorgenfrei, K. Watanabe, T. Taniguchi, P. Kim, K. L. Shepard, and J. Hone, *Nat. Nanotechnol.* **5**, 722 (2010).
- [4] B. Radisavljevic, A. Radenovic, J. Brivio, V. Giacometti, and A. Kis, *Nat. Nanotechnol.* **6**, 147 (2011).
- [5] K. S. Novoselov, D. Jiang, T. J. Booth, W. Khotkevich, S. V. Morozov, and A. K. Geim, *Proc. Natl. Acad. Sci. USA* **102**, 10451 (2005).
- [6] Q. H. Wang, K. Kalantar-Zadeh, A. Kis, J. N. Coleman, and M. S. Strano, *Nat. Nanotechnol.* **7**, 699 (2012).
- [7] T. Heine, *Acc. Chem. Res.* **48**, 65 (2015).
- [8] W. Zhang and W. Ji, *Phys. Chem. Chem. Phys.* **22**, 24662 (2020).
- [9] M. Gao, W. Zhang, and L. Zhang, *Nano Lett.* **18**, 4424 (2018).
- [10] J. Zhang, S. Jia, I. Kholmanov, L. Dong, D. Er, W. Chen, H. Guo, Z. Jin, V. B. Shenoy, L. Shi, and J. Lou, *ACS Nano* **11**, 8192 (2017).
- [11] A. Lu, H. Zhu, J. Xiao, C. Chuu, Y. Han, M. Chiu, C. C. Cheng, C. Yang, K. Wei, Y. Yang, Y. Wang, D. Sokaras, D. Nordlund, P. Yang, D. Muller, M. Y. Chou, X. Zhang, and L. Li, *Nat. Nanotechnol.* **12**, 744 (2017).
- [12] Z. Wang and G. Zhou, *J. Phys. Chem. C* **124**, 167 (2020).
- [13] L. Ju, M. Bie, X. Tang, J. Shang, and L. Z. Kou, *ACS Appl. Mater. Interfaces* **12**, 40794 (2020).
- [14] M. Yagmurcukardes, C. Sevik, and F. M. Peeters, *Phys. Rev. B* **100**, 045415 (2019).
- [15] Z. Guan, S. Ni, and S. Hu, *J. Phys. Chem. C* **122**, 6209 (2018).
- [16] R. Peng, Y. Ma, B. Huang, and Y. Dai, *J. Mater. Chem. A* **7**, 603 (2019).
- [17] R. Sant, M. Gay, A. Marty, S. Lisi, R. Harrabi, C. Vergnaud, M. T. Dau, X. Weng, J. Coraux, N. Gauthier, O. Renault, G. Renaud, and M. Jamet, *npj 2D Mater. Appl.* **4**, 41 (2020).
- [18] Y. Chu, J. Zhong, H. Liu, Y. Ma, N. Liu, Y. Song, J. Liang, Z. Shao, Y. Sun, Y. Dong, X. Wang, and L. Lin, *Adv. Funct. Mater.* **28**, 1803413 (2018).
- [19] Y. Cheng, Y. Ma, L. Li, M. Zhu, Y. Yue, W. Liu, L. Wang, S. Jia, C. Li, T. Qi, J. Wang, and Y. Gao, *ACS Nano* **14**, 2145 (2020).
- [20] Y. Ji, M. Yang, H. Lin, T. Hou, L. Wang, Y. Li, and S.-T. Lee, *J. Phys. Chem. C* **122**, 3123 (2018).
- [21] J. Wu, H. Lin, D. Moss, K. Loh, and B. Jia, *Nat. Rev. Chem.* **7**, 162 (2023).
- [22] J. Lu, X. Zhang, G. Su, W. Yang, K. Han, X. Yu, Y. Wan, X. Wang, and P. Yang, *Mater. Today Phys.* **18**, 100376 (2021).
- [23] M. van Spronsen, J. Frenken, and I. Groot, *Nat. Commun.* **8**, 429 (2017).
- [24] H. Shen, Y. Zhang, G. Wang, W. Ji, X. Xue, and W. Zhang, *Phys. Chem. Chem. Phys.* **23**, 21825 (2021).
- [25] X. Ge, X. H. Zhou, D. Y. Sun, and X. S. Chen, *ACS Omega* **8**, 5715 (2023).
- [26] S. Bertolazzi, J. Brivio, and A. Kis, *ACS Nano* **5**, 9703 (2011).
- [27] W. Zhang, H. Guo, J. Jiang, Q. Tao, X. Song, H. Li, and J. Huang, *J. Appl. Phys.* **120**, 013904 (2016).
- [28] W. Zhang, A. Srivastava, X. Li, and L. Zhang, *Phys. Rev. B* **102**, 174301 (2020).
- [29] Z. Ni, T. Yu, Y. Lu, Y. Wang, Y. Feng, and Z. Shen, *ACS Nano* **2**, 2301 (2008).
- [30] P. E. Blöchl, *Phys. Rev. B* **50**, 17953 (1994).
- [31] G. Kresse and J. Furthmüller, *Phys. Rev. B* **54**, 11169 (1996).
- [32] G. Kresse and D. Joubert, *Phys. Rev. B* **59**, 1758 (1999).
- [33] J. P. Perdew, K. Burke, and M. Ernzerhof, *Phys. Rev. Lett.* **77**, 3865 (1996).
- [34] H. J. Monkhorst and J. D. Pack, *Phys. Rev. B* **13**, 5188 (1976).
- [35] S. Grimme, J. Antony, S. Ehrlich, and S. Krieg, *J. Chem. Phys.* **132**, 154104 (2010).
- [36] S. Grimme, S. Ehrlich, and L. Goerigk, *J. Chem. Phys.* **32**, 1456 (2011).
- [37] A. Togo and I. Tanaka, *Scr. Mater.* **108**, 1 (2015).
- [38] W. L. Tao, Y. Mu, C. E. Hu, Y. Cheng, and G. F. Ji, *Philos. Mag.* **99**, 1025 (2019).
- [39] S. D. Guo, X. S. Guo, and Y. Deng, *J. Appl. Phys.* **126**, 154301 (2019).
- [40] H. L. Zhuang and R. G. Hennig, *J. Phys. Chem. C* **117**, 20440 (2013).
- [41] See Supplemental Material at <http://link.aps.org/supplemental/10.1103/PhysRevB.108.035411> for structural parameters and other basic properties of PtXO; the comparisons of Raman frequencies with experiments of PtX₂ and the expected experimental Raman frequencies of PtXO; the elements of Raman tensor of A_1^O and E^O in PtXO; the *ab initio* molecular dynamics calculations of strained PtXO; the evolution of bond length with respect to the strain; Raman activity of PtXO at a large strain of 10%; and stacking patterns and binding energy of bilayer PtXO.
- [42] Bilbao Crystallographic Server, <https://www.cryst.ehu.es>.
- [43] Y. Zhao, J. Qiao, P. Yu, Z. Hu, Z. Lin, S. Lau, Z. Liu, W. Ji, and Y. Chai, *Adv. Mater.* **28**, 2399 (2016).
- [44] Y. Zhao, J. Qiao, Z. Yu, P. Yu, K. Xu, S. Lau, W. Zhou, Z. Liu, X. Wang, W. Ji, and Y. Chai, *Adv. Mater.* **29**, 1604230 (2017).
- [45] C. Rice, R. J. Young, R. Zan, U. Bangert, D. Wolverson, T. Georgiou, R. Jalil, and K. S. Novoselov, *Phys. Rev. B* **87**, 081307(R) (2013).
- [46] M. Yagmurcukardes, C. Bacaksiz, E. Unsal, B. Akbali, R. T. Senger, and H. Sahin, *Phys. Rev. B* **97**, 115427 (2018).
- [47] S. D. Guo, X. Guo, Z. Liu, and Y. Quan, *J. Appl. Phys.* **127**, 064302 (2020).
- [48] S. D. Guo, X. S. Guo, R. Y. Han, and Y. Deng, *Phys. Chem. Chem. Phys.* **21**, 24620 (2019).
- [49] M. N. Blonsky, H. L. Zhuang, A. K. Singh, and R. G. Hennig, *ACS Nano* **9**, 9885 (2015).
- [50] G. Henkelman, A. Arnaldsson, and H. Jonsson, *Comput. Mater. Sci.* **36**, 354 (2006).